Numerical dynamo simulations reproduce palaeomagnetic field behaviour

D. G. Meduri[1], A. J. Biggin[1], C. J. Davies[2], R. K. Bono[1], C. J. Sprain[3], J. Wicht[4]

[1]Department of Earth, Ocean and Ecological Sciences, University of Liverpool, Liverpool, UK
[2]School of Earth and Environment, University of Leeds, Leeds, UK
[3]Department of Geological Sciences, University of Florida, Gainesville, FL, USA
[4]Department Planets and Comets, Max Planck Institute for Solar System Research, Göttingen, Germany

Key Points:

- We present the first numerical geodynamo simulations known to reproduce the main features of palaeomagnetic field variability since 10 Ma
- All simulated characteristics of palaeomagnetic behaviour covary with the degree of dipole dominance (dipolarity)
- Only chemically driven dynamos at sufficiently low Ekman numbers in a specific dipolarity range capture all palaeomagnetic characteristics

Corresponding author: Domenico G. Meduri, domenico.meduri@liverpool.ac.uk

Abstract

Numerical geodynamo simulations capture several features of the spatial and temporal geomagnetic field variability on historical and Holocene timescales. However, a recent analysis questioned the ability of these numerical models to comply with long-term palaeomagnetic field behaviour. Analysing a suite of 50 geodynamo models, we present here the first numerical simulations known to reproduce all salient aspects of the palaeosecular variation and time-averaged field behaviour since 10 Ma. We find that the simulated field characteristics covary with the relative dipole field strength at the core-mantle boundary (dipolarity). Only models which, in addition to compositional driving, have an Ekman number (ratio of viscous to Coriolis forces) lower than 10^{-3} and a dipolarity in the range $0.34-0.56$ capture the palaeomagnetic field behaviour to a high level. Our findings well agree with dipolarity estimates obtained from state-of-the-art statistical field models and represent a testable prediction for next generation global palaeomagnetic field reconstructions.

Plain Language Summary

Earth's magnetic field varies on a wide range of timescales, from less than a year to hundreds of million years or longer. Such variations are produced by the complex fluid dynamic processes in the liquid iron core, which are generally studied using 3D computer simulations. While these simulations reproduced several properties of the observed magnetic field behaviour on relatively short timescales (less than 10 kyr), their compliance with the field characteristics on longer timescales has been recently questioned. Here we present the first simulations known to reproduce all salient features of Earth's magnetic field behaviour over the last 10 Myr. Analysing a large suite of simulations, we discovered that the most Earth-like ones, in addition to having buoyancy sources that model the release of light elements from the inner core, have to rotate fast enough and have a magnetic field morphology which is sufficiently, but not too strongly, dipolar. These results well agree with independent estimates of the degree of dipole dominance obtained from observational models. Our findings will be used by future studies to simulate reliably long-term Earth's magnetic field behaviour, hence improving our understanding of the Earth's core and its evolution.

1 Introduction

The geomagnetic field varies on a striking range of spatial and temporal scales. These variations can be characterised through direct observations only for the last four centuries, while on longer timescales information is available indirectly through palaeomagnetic and archaeomagnetic measurements. By tying together observations and numerical simulations of the dynamo process in the outer core, we can gain fundamental insights into the physics of the deep interior through geologic time.

Numerical dynamo simulations reproduced several features of the geomagnetic field, including a dipole-dominated field and polarity reversals (see, e.g., Christensen & Wicht, 2015), the fundamental time-averaged morphological properties of the historical field (Christensen, 2010), and the axial dipole variations observed over Holocene timescales (Davies & Constable, 2014). However, due to the current computational limitations, geodynamo simulations cannot run at the extreme conditions that characterise the turbulent core fluid. Such limitations are particularly severe when studying the long-term field behaviour, since long time integrations are needed. Recently, Sprain et al. (2019) (S19 hereafter) raised the question of how Earth-like was the long-term field behaviour displayed by dynamo simulations. Defining a set of criteria ($Q_{\rm PM}$ criteria) to quantify the degree of semblance of geodynamo simulations with the palaeomagnetic field of the last 10 Myr, they found that none of the 46 simulations explored could capture all aspects of the observed variability. In fact, only a few simulations passed three out of the five Q_{PM} criteria, while the large majority performed poorly.

Here we present a different set of simulations that faithfully reproduce the palaeomagnetic field over the last 10 Myr in terms of the Q_{PM} criteria. We show that the relative strength of the dipole field at the core-mantle boundary (CMB) can be used as a proxy for all the palaeomagnetic observables considered and we discuss the conditions necessary for obtaining palaeomagnetic-like simulations.

2 Methods

2.1 Model Formulation

The setup and solution method for the geodynamo models are standard and extensively documented elsewhere (Willis et al., 2007; Davies & Constable, 2014; Wicht, 2002; Wicht & Meduri, 2016). We therefore provide only a brief description here (see also Section S1). We consider a convection-driven magnetohydrodynamic flow under the Boussinesq approximation with the fluid confined to a spherical shell of thickness $d = r_{\mathrm{o}} - r_{\mathrm{i}}$ rotating at a constant angular velocity Ω. Here r_{i} and r_{o} are the inner and outer boundary radii, which are identified with the inner core radius and the CMB radius, respectively.

All models assume no slip mechanical boundary conditions and an electrically insulating mantle. We employ the codensity approach where density perturbations due to compositional and temperature differences are described by only one variable. Different convective driving scenarios are modelled via the boundary conditions and eventual codensity sinks. Thermal dynamos are bottom heated with either fixed flux or fixed temperature at r_{i}. The heat leaves the system through r_{o} where a fixed flux condition is imposed. Some models employ lateral variations in the outer boundary heat flux in the form of a recumbent spherical harmonic (SH) of degree $\ell = 2$ and order $m = 0$ as an approximation of the observed shear-wave structures (Dziewonski et al., 2010).

Chemical dynamos are driven by either a fixed light elements concentration or concentration gradient at r_{i} that is balanced by a volumetric mass sink. The flux through r_{o} is set to zero since the incorporation of light elements into the mantle matrix is very inefficient. While the chemical dynamos have an electrically conducting inner core, the thermal dynamos use an insulating inner core for simplicity. Wicht (2002) showed that the impact of inner core conductivity on the magnetic field and its variability is minor.

The dimensionless parameters controlling the system are the Ekman number Ek, the Prandtl number Pr, the magnetic Prandtl number Pm and the shell aspect ratio χ:

$$\mathrm{Ek} = \frac{\nu}{\Omega d^2}, \quad \mathrm{Pr} = \frac{\nu}{\kappa} = 1, \quad \mathrm{Pm} = \frac{\nu}{\eta}, \quad \chi = \frac{r_{\mathrm{i}}}{r_{\mathrm{o}}} = 0.35. \tag{1}$$

Here ν, η and κ are the kinematic viscosity, magnetic diffusivity and thermal (or compositional) diffusivity of the fluid, respectively. The Rayleigh number controls the vigour of convection and is defined in Section S1. Ek varies between 3×10^{-4} and 2×10^{-3}, and Pm spans the range $3 - 10$. These ranges are constrained by the need to perform long temporal integrations.

Our dataset is summarised in Table S1 and consists of 50 simulations: 21 from S19, 7 from Wicht and Meduri (2016) and 22 are new runs. From S19 we excluded thermal dynamos which use specific buoyancy profiles (Davies & Gubbins, 2011), large amplitudes of the CMB heat flux anomalies ($\epsilon = 1.5$; see Table S1 for the definition of ϵ) and low Rayleigh numbers (regime of locked dynamo action). We also excluded the cases at $\mathrm{Pm} = 20$. All these simulations poorly comply with Earth having total Q_{PM} misfits larger than 5 and total Q_{PM} scores of 3 at most (see Section 2.2).

2.2 Palaeomagnetic Criteria for Geodynamo Simulations

The $Q_{\rm PM}$ framework is described in detail in S19 and we recall only the essentials here. S19 identified five palaeomagnetic observables that describe the long-term palaeosecular variation (PSV) and time-averaged field (TAF) behaviour. The first two observables characterise the virtual geomagnetic pole (VGP) angular dispersion S by estimating its equatorial value and latitudinal dependence. They are the parameters a and b of the empirical quadratic fit with palaeolatitude λ introduced by McFadden et al. (1988),

$$S^2 = a^2 + (b\lambda)^2. \tag{2}$$

The third $Q_{\rm PM}$ observable is the absolute maximum of the inclination anomaly

$$\Delta I = \bar{I} - I_{GAD}, \tag{3}$$

which is function of latitude. Here $\bar{I}$ is the Fisher mean inclination (Fisher, 1953) and I_{GAD} is the inclination expected under a geocentric axial dipole field. The fourth observable, $V\%$, is the ratio of the interquartile range to the median of the virtual dipole moment (VDM) distribution. The last observable is the relative transitional time $\tau_{\rm T}$, defined as the fraction of time spent with an absolute true dipole latitude lower than 45°, which is complemented with a criterion on the presence of reversals.

S19 estimated values of these five observables for the last 10 Myr using PSV10, the most recent compilation of palaeomagnetic directional data (Cromwell et al., 2018), and the palaeointensity database PINT (Biggin et al., 2009, 2015). The sum of normalised linear misfits between simulated and observed values for each $Q_{\rm PM}$ observable is $Q^{\rm m}_{\rm PM}$ ($\Delta Q_{\rm PM}$ in S19). If the misfit of a given $Q_{\rm PM}$ observable is ≤ 1, the observed and simulated palaeomagnetic characteristic overlap within the respective estimated uncertainties. The larger the total misfit $Q^{\rm m}_{\rm PM}$, the worse a numerical simulation complies with Earth.

Together with the misfits, S19 defined binary scores. The score of a given $Q_{\rm PM}$ observable is 1 if the misfit in that observable is ≤ 1 and is zero otherwise. The total score $Q^{\rm s}_{\rm PM}$, obtained by summing the single $Q_{\rm PM}$ scores, can range from 0 to 5. By definition, a palaeomagnetic-like simulation with the maximum score $Q^{\rm s}_{\rm PM} = 5$ has a total misfit $Q^{\rm m}_{\rm PM} \leq 5$. Note that the converse is not true: simulations with $Q^{\rm m}_{\rm PM} \leq 5$ can have $Q^{\rm s}_{\rm PM} < 5$ because not all the simulated and observed palaeomagnetic characteristics overlap within their uncertainties.

3 Results

3.1 Evidence for Palaeomagnetic-Like Geodynamo Simulations

The magnetic fields obtained in geodynamo simulations are generally characterised by their degree of dipole dominance, which is often measured by the dipolarity D_{12}, defined as the time-averaged ratio of the root mean square (RMS) dipole field strength at the CMB to the total RMS field strength up to SH degree and order $\ell = m = 12$ (Christensen & Aubert, 2006). Multipolar solutions generally have $D_{12} \lesssim 0.35$, while dominantly dipolar ones like the present geomagnetic field have $D_{12} > 0.7$ (Christensen & Aubert, 2006; Christensen, 2010). Earth-like reversing solutions, that is dynamos which are dipole dominated most of the time but occasionally undergo reversals, occur in a narrow dipolarity range sandwiched between the stable dipolar and the multipolar regimes (Driscoll & Olson, 2009; Wicht & Tilgner, 2010; Wicht et al., 2015).

Figures 1a,c demonstrate that D_{12} is a valid proxy for the total misfit $Q^{\rm m}_{\rm PM}$. When the Rayleigh number increases (in the direction indicated by the arrows in the connected lines in Figure 1) the dipolarity systematically decreases together with $Q^{\rm m}_{\rm PM}$ until $D_{12} < 0.5$ when $Q^{\rm m}_{\rm PM}$ increases again so that the simulations describe parabolic paths in the

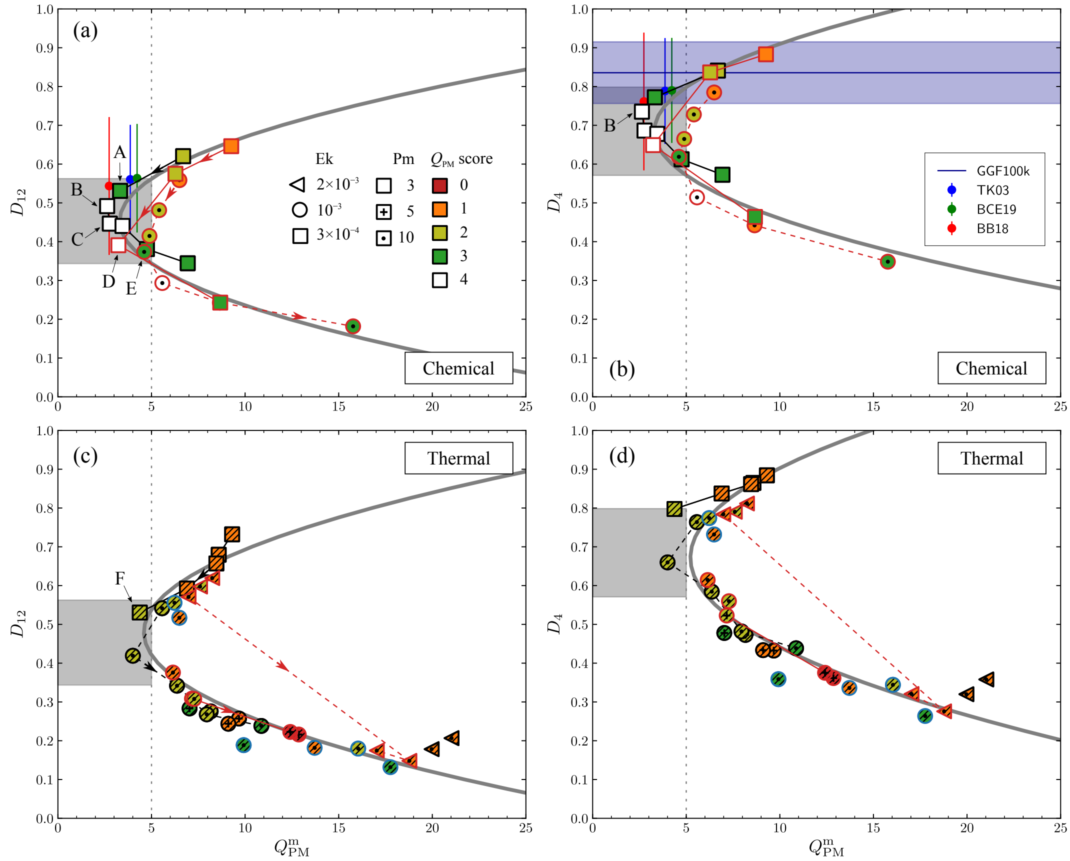

Figure 1. (a,c) Dipolarity D_{12} as function of the total misfit $Q_{\mathrm{PM}}^{\mathrm{m}}$ for (a) chemical and (c) thermal (hatched symbols) dynamos. The symbol shape and colour code the Ekman number Ek and the total Q_{PM} score respectively (see the legend inset). The marker inside the main symbol indicates the magnetic Prandtl number Pm. The symbol rim colour denotes the codensity boundary conditions (black: fixed temperature/codensity at r_{i}; red: fixed temperature/codensity flux at r_{i}; blue: presence of lateral heat flux variations at r_{o}). Connecting lines show dynamos differing only in the Rayleigh number, which increases in the direction indicated by the arrows. For clarity, only four representative Rayleigh number tracks are presented in (c) and (d). The thick curves show quadratic fits to the chemical dynamos at Ek $= 3 \times 10^{-4}$ and to all thermal dynamos. The grey rectangle highlights the region of palaeomagnetic-like dynamos defined by the chemical models (the vertical extent of this region is ΔD_{12}; see the main text for further explanations). (b,d) Same as (a) and (c) but for the modified dipolarity D_4. The horizontal blue line in (b) shows the global palaeomagnetic field model GGF100k, with the shaded region indicating the intervals of one standard deviation above and below D_4. Circles with error bars in (a) and (b) present three GGP models indicated in the legend inset in (b) (the error bars denote intervals of one standard deviation above and below D_4). Capital letters A–F mark six simulations discussed in the main text (see Table S1).

$Q^{\rm m}_{\rm PM}$-D_{12} plane. These paths present only a mild dependence on Pm and on the thermal boundary conditions, but depend strongly on the Ekman number. In fact, chemical dynamos at Ek $= 3 \times 10^{-4}$ reach the lowest misfits, whereas runs at Ek $= 10^{-3}$ only border on the Earth-like region defined by misfits $Q^{\rm m}_{\rm PM} < 5$ (Figure 1a). Our chemical dynamos at 3×10^{-4} do not have a total $Q_{\rm PM}$ score of 5, but are extremely close to satisfying all criteria (see Section 3.2). While chemical dynamos can have $Q^{\rm m}_{\rm PM}$ as low as 2.7 with $Q^{\rm s}_{\rm PM} = 4$, thermal dynamos hardly reach $Q^{\rm m}_{\rm PM} \approx 4$ with $Q^{\rm s}_{\rm PM} = 2$ (Figure 1c). The quadratic function $Q^{\rm m}_{\rm PM} = c_0 + c_1 D_{12} + c_2 (D_{12})^2$ well describes the simulations behaviour in both types of convective forcing (grey curves in Figures 1a,c; see Table S2 for the regression coefficients values). The high coefficients of determination, $R^2 = 0.85$ and $R^2 = 0.79$ for the chemical and the thermal dynamos respectively, confirm the robustness of this empirical quadratic fit.

Remarkably, the optimal value of D_{12}, that is the one which yields the lowest $Q^{\rm m}_{\rm PM}$ and the highest $Q^{\rm s}_{\rm PM}$, lies in a well defined range for all Rayleigh number tracks explored. The minima of the quadratic fits occur at $D_{12} = 0.45$ and $D_{12} = 0.48$ for the chemical and the thermal dynamos respectively. Small departures from these values cause a large increase of $Q^{\rm m}_{\rm PM}$ and a decrease in $Q^{\rm s}_{\rm PM}$. The values of D_{12} where the quadratic fit of the chemical dynamos at Ek $= 3\times10^{-4}$ intersects the threshold $Q^{\rm m}_{\rm PM} = 5$ define the dipolarity interval $\Delta D_{12} = [0.34, 0.56]$ where palaeomagnetic-like dynamos can be found.

The dipolarity values of our palaeomagnetic-like dynamos are compatible with estimates obtained for Earth from global palaeomagnetic field model reconstructions. These models have spatial power spectra that are generally considered to be well resolved only up to SH degree $\ell = 4$ (Korte & Constable, 2008; Wardinski & Korte, 2008; Nilsson et al., 2014), hence we consider the modified dipolarity D_4 which is defined up to $\ell = m = 4$. Figures 1b,d show that the quadratic fit to D_{12} can also describe the behaviour of D_4 in our numerical simulations. The palaeomagnetic-like region predicted by our chemical dynamos at Ek $= 3\times10^{-4}$ is $\Delta D_4 = [0.57, 0.80]$. GGF100k (Panovska et al., 2018), the longest global field reconstruction to date spanning the last 100 kyr, provides $D_4 = 0.84\pm0.08$, which is in relatively good agreement with our numerical predictions (Figure 1b; see also Table S3). LSMOD.2 (Brown et al., 2018) has a lower value of $D_4 = 0.74$ since it deliberately models the field during the two most recent excursions. This lower estimate is in excellent agreement with the value obtained for run B, our most palaeomagnetic-like simulation, and generally compatible with the runs in the palaeomagnetic-like region of Figure 1b (see also Table S3). For field reconstructions covering shorter time intervals, the Holocene CALS10k.1b (Korte et al., 2011) and the historical gufm1 (Jackson et al., 2000) models provide $D_4 = 0.92$ and 0.88 respectively. Such high values of D_4 are likely due to the short timescales sampled by these models. We remark here that all the observational models cover timescales much shorter than the last 10 Myr and differences with our numerical predictions of D_4 are inevitable. It is encouraging that such differences reduce when considering the longer time averages obtained from GGF100k and LSMOD.2.

Estimates of D_{12} for Earth on timescales of million years can be obtained from statistical magnetic field models based on a giant Gaussian process (GGP). Here we consider the GGP models TK03 (Tauxe & Kent, 2004), BCE19 (Brandt et al., 2020) and BB18 (Bono et al., 2020), which are explicitly constructed to reproduce the PSV over the last $5-10$ Myr, with BB18 also capturing the observed VDM distribution. TK03 and BCE19 differ only in the assumed variances of their independent and normally distributed Gauss coefficients, while BB18 additionally employs a covariance pattern for degrees $\ell \leq 4$ inferred from dynamo simulations. The three GGP models all have $0.54 \leq D_{12} \leq 0.56$ and thus fall into the palaeomagnetic-like region predicted by our numerical simulations (see Figure 1a and also Table S3). This is because the power spectra of the GGP models decay with degree ℓ at a rate comparable with the numerical simulations, as demonstrated by the similar variation in the dipolarity values obtained for different degrees of truncation (Figure S1).

3.2 Description of the Simulated Long-Term Field Behaviour

3.2.1 Variation of the Palaeomagnetic Observables With D_{12}

Figures 2a–e present D_{12} as a function of the different Q_{PM} observables for all the chemical dynamos. All observables increase as D_{12} decreases, a trend which is also observed for the thermal dynamos (Figure S2). To capture the excursional and reversal behaviour expected for Earth, our three most palaeomagnetic-like chemical dynamos (runs B, C and D in Figure 1a) suggest that a compromise between the equatorial dispersion a and the relative transitional time τ_{T} must be reached. Run B satisfies all Q_{PM} criteria (Figures 2a–d; cf. also Table S3), except τ_{T} which is too small at 1.8% since the field undergoes only one reversal and three brief excursions in more than 35 magnetic diffusion times. Runs C and D, on the other hand, show an Earth-like transitional time ($\tau_{\mathrm{T}} =$ 4.6% and 6.5% respectively; Figure 2e), but a less realistic equatorial dispersion, which is slightly too high (Figure 2a). The lower confidence bounds of a of these latter runs differ from the upper confidence bound of the Earth by only 1° and 2° respectively (Tables S3 and S4) and we therefore consider these simulations definitely consistent with Earth's palaeomagnetic field.

3.2.2 Influence of the Ekman Number in Chemical Dynamos

As well as intermediate values of D_{12}, chemical dynamos can reach low misfits and high scores only if the Ekman number is low enough (Figure 1a). This dependency on Ek arises from differences in the behaviour of a and of τ_{T}. In the palaeomagnetic-like dipolarity interval ΔD_{12} chemical dynamos at $\mathrm{Ek} = 10^{-3}$ have generally higher a and lower τ_{T} than the cases at the lower Ek of $3{\times}10^{-4}$ (Figures 2a,e). Misfits in a and τ_{T} are indeed up to three times larger for the high-Ek runs compared to the low-Ek cases, while misfits in the other Q_{PM} observables are not very different (in Table S3 compare, for example, run D with run E, the simulation with the lowest total misfit at $\mathrm{Ek} = 10^{-3}$).

In the high-Ek simulations, more frequent polarity transitions leading to Earth-like values of τ_{T} start at $D_{12} \approx 0.3$, but a is far too high (see Figure 3a). On the contrary, the onset of reversals occurs at higher values of D_{12} at $\mathrm{Ek} = 3 \times 10^{-4}$ where a is still Earth-like. Such a dependency on Ek for the onset of reversals was also observed in previous investigations of chemically driven dynamos (Driscoll & Olson, 2009). The onset of reversals at higher values of D_{12} arises because the variability in field strength, measured by the relative standard deviation $\sigma_B/\overline{B}$ (the ratio of the standard deviation of the total RMS field strength at the CMB to its time-averaged value), increases with decreasing Ek in our simulations (Figure 3b). Such larger temporal fluctuations are more likely to drive the CMB field strength towards lower intensities, which in turn lead to an increased likelihood of both transitional periods and polarity transitions (Driscoll & Olson, 2009). Despite these larger field fluctuations, a remains Earth-like in the low-Ek runs since the equatorially symmetric CMB field, which determines a (McFadden et al., 1988; Coe & Glatzmaier, 2006), has a generally lower amplitude compared to the high-Ek cases (Figure S3).

3.2.3 Influence of the Convective Driving Mode

Thermal dynamos at $\mathrm{Ek} = 3{\times}10^{-4}$ do not reach $Q^{\mathrm{m}}_{\mathrm{PM}}$ as low, and $Q^{\mathrm{s}}_{\mathrm{PM}}$ as high, as the chemical dynamos at the same Ekman number (Section 3.1). This is due to the latitudinal VGP dispersion b, which remains fairly low and non-Earth-like in the thermal dynamos for all D_{12} explored (Figure 3c). The weak variation of b with D_{12} can be ascribed to the almost constant odd and even CMB field contributions in these runs (Fig-

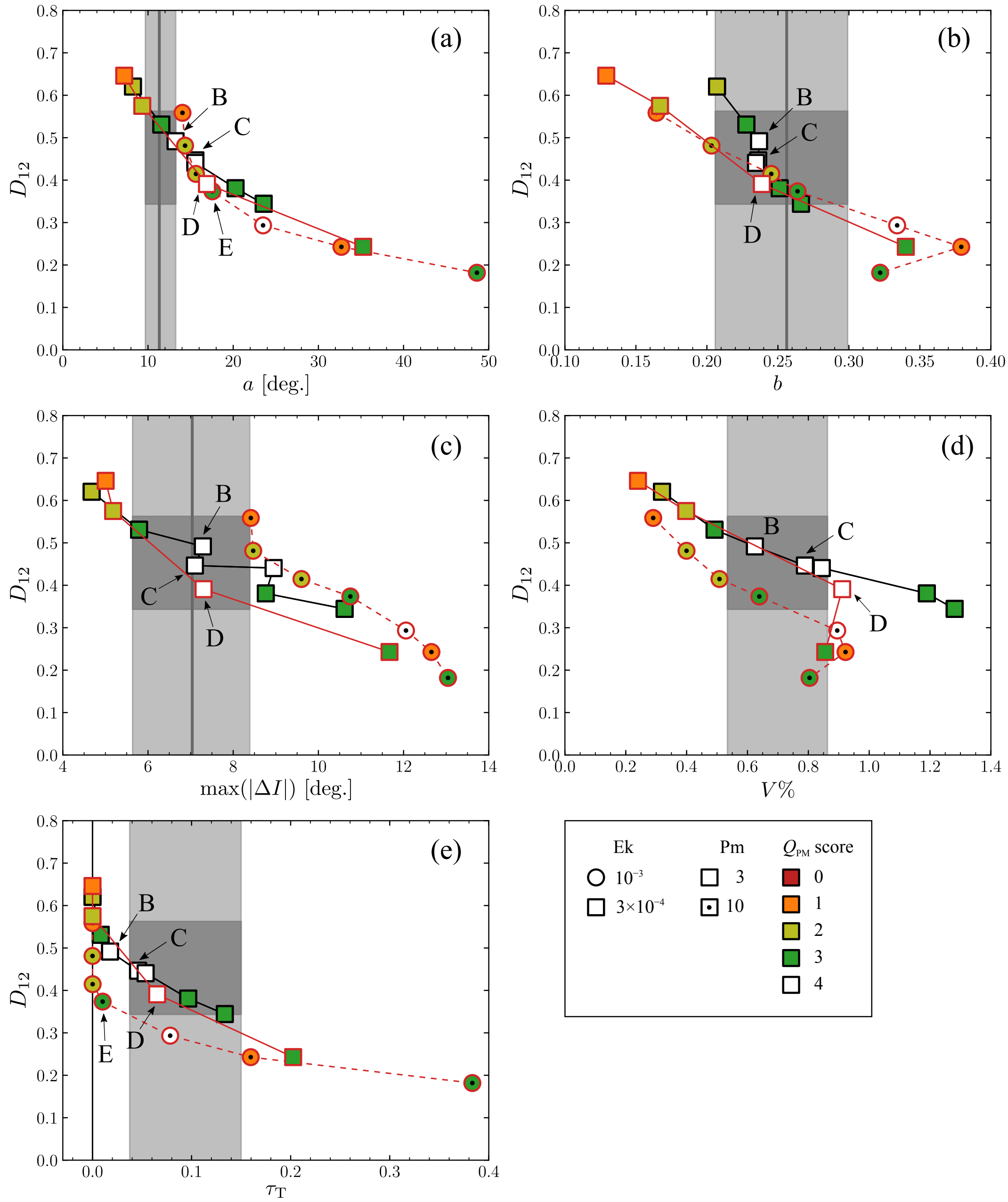

Figure 2. Dipolarity D_{12} as function of the five $Q_{\rm PM}$ observables for the chemical dynamos. Connecting lines indicate Rayleigh number tracks as in Figure 1a (the Rayleigh number increases for decreasing D_{12}). For the meaning of the symbols, see the legend at the bottom right and Figure 1. Vertical grey regions denote the estimated values for Earth (medians as solid lines and shaded regions indicating the 95% confidence intervals or the assumed bounds). The dark grey rectangle highlights the palaeomagnetic-like dipolarity interval ΔD_{12} defined as explained in the main text.

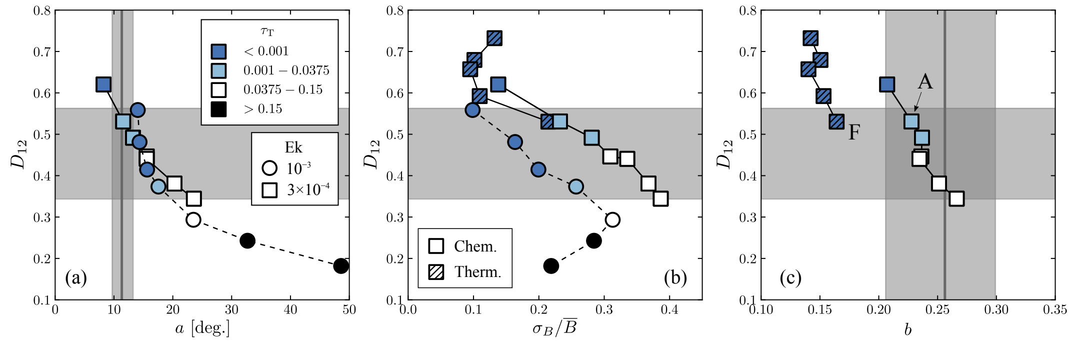

Figure 3. Dipolarity D_{12} as function of (a) the equatorial VGP dispersion a, (b) the relative standard deviation of the CMB field strength $\sigma_B/\overline{B}$ and (c) the latitudinal VGP dispersion b for three selected Rayleigh number tracks (only two tracks shown in (c) for clarity). The Rayleigh number increases for decreasing D_{12}. Chemical dynamo tracks are those at Ek $= 3 \times 10^{-4}$ with fixed flux at r_i and at Ek $= 10^{-3}$ (see Figures 1 and 2). The thermal dynamo track is the one at Ek $= 3 \times 10^{-4}$ in Figures 1 and S2. The symbol colour codes the relative transitional time τ_T as indicated in the legend inset in (a) (Earth-like τ_T according to Q_PM criteria in white). Vertical grey shaded regions in (a) and (c) denote the values of a and b estimated for Earth as in Figures 2a,b. The horizontal grey region marks the palaeomagnetic-like dipolarity interval ΔD_{12}.

ure S3). All the other Q_PM observables show similar variations with D_{12} between the two convective driving modes (Figure S2).

The onset of reversals at Ek $= 3{\times}10^{-4}$ may occur at larger values of D_{12} in the chemical dynamos compared to the thermal ones and this contributes to the lower Q^m_PM reached by the chemical models at intermediate dipolarities. For example, while run F (thermal) shows a stable dipole tilt with $\tau_\mathrm{T} = 0$, run A (chemical) has a higher activity with few excursions and $\tau_\mathrm{T} = 1\%$ (Figure 3c; see also Figure S2e). We caveat here that the thermal dynamos have an electrically insulating inner core, while the chemical dynamos have a conducting one and this may have an impact on the occurrence of excursions and reversals and on the behaviour of the field at low intensities (Lhuillier et al., 2013).

4 Discussion and Conclusions

Applying the Q_PM framework of S19, we presented the first numerical geodynamo simulations known to reproduce the fundamental aspects of the palaeomagnetic field behaviour since 10 Ma. We found that the dipolarity D_{12}, which measures the degree of dipole dominance at the CMB, is a good proxy for all five Q_PM observables. Moreover, D_{12} allows predictions of the total Q_PM misfit and score across a variety of simulations differing in control parameters, boundary conditions and convective driving mode. Simulations reproducing all aspects of the observed palaeomagnetic field behaviour need to (i) be purely chemically driven, (ii) have Ek below 10^{-3} and (iii) have a dipolarity D_{12} which falls in the interval $\Delta D_{12} = [0.34, 0.56]$. These conditions can be readily used to assess the compliance of existing simulations with the palaeomagnetic field since 10 Ma. Future studies should employ only simulations that fulfil such conditions to make inferences about the palaeomagnetic field on long timescales.

The palaeomagnetic-like dipolarity interval ΔD_{12} is bounded above by the modern field and below by the multipolar dynamo regime. Current GGP models provide estimates of D_{12} for Earth of about 0.55, which agrees very well with our numerical simulation results. These results represent a specific, testable prediction for next generation global field reconstructions, once they reach higher spatial resolutions and cover longer time intervals than the models currently available. The lower bound of ΔD_{12} marks the transition to the multipolar dynamo regime, which occurs at $D_{12} = 0.35-0.50$ (Christensen & Aubert, 2006; Oruba & Dormy, 2014). These studies suggested that the Earth's core lies at the transition between the two dynamo regimes and our results are compatible with these findings.

Our results suggest the possibility of constructing a path towards Earth's core conditions which preserves palaeomagnetic-like dynamo characteristics. According to Oruba and Dormy (2014), the parameter combination $\mathrm{Re}\,\mathrm{Ek}^{2/3}$ ($\mathrm{Re} = \mathrm{U}d/\nu$ is the Reynolds number, where U is the time-averaged RMS core flow velocity) defines the dipolar-multipolar transition at $D_{12} \approx 0.5$, which is close to the optimal value of D_{12} inferred from our analysis. To maintain a constant value of D_{12} while reducing Ek, Re needs to increase and this can be achieved by increasing the Rayleigh number and by decreasing Pm. Following this path to lower Ek and Pm and higher Rayleigh numbers, the relevant balance for the Earth's core between magnetic, Coriolis and buoyancy forces is expected to emerge naturally, as also suggested by recent high-resolution numerical simulations (Yadav et al., 2016; Schaeffer et al., 2017; Aubert et al., 2017).

Taken at face value, our analysis appears to favour compositional over thermal convection as the dominant driving mode of the geodynamo over the last 10 Myr. This is consistent with theoretical analyses based on both thermal history calculations (see, e.g., Nimmo, 2015) and numerical dynamo studies (Kutzner & Christensen, 2000). Future work should address the validity of this result with simulations at more extreme conditions than what explored here.

Acknowledgments

The simulation output data used to produce Figures 1–3 can be found in the supplementary information (Tables S1–S5). The data will be available in the OSF repository by acceptance. Funding for DGM, AJB, and RKB was provided by The Leverhulme Trust Research Leadership Award, RL-2016-080; for CJD, by the NERC fellowship NE/L011328/1. AJB additionally acknowledges funding from NERC Standard Grant NE/P00170X/1. The authors declare no competing financial interests. A portion of the geodynamo simulations were performed on the UK National Supercomputing Service ARCHER and on ARC, part of the High Performance Computing facilities at the University of Leeds, UK.

References

Aubert, J., Gastine, T., & Fournier, A. (2017). Spherical convective dynamos in the rapidly rotating asymptotic regime. *Journal of Fluid Mechanics*, *813*, 558?593. doi: 10.1017/jfm.2016.789

Biggin, A. J., Piispa, E. J., Pesonen, L. J., Holme, R., Paterson, G. A., Veikkolainen, T., & Tauxe, L. (2015). Palaeomagnetic field intensity variations suggest mesoproterozoic inner-core nucleation. *Nature*, *526*, 245?248. doi: https://doi.org/10.1038/nature15523

Biggin, A. J., Strik, G. H. M. A., & Langereis, C. G. (2009). The intensity of the geomagnetic field in the late-archaean: new measurements and an analysis of the updated iaga palaeointensity database. *Earth, Planets and Space*, *61*, 9-22. doi: https://doi.org/10.1186/BF03352881

Bono, R. K., Biggin, A. J., Holme, R., Davies, C. J., Meduri, D. G., & Bestard, J. (2020). Covariant giant gaussian process models with improved reproduction of palaeosecular variation. *Geochemistry, Geophysics, Geosystems*, *21*(8), e2020GC008960. doi: 10.1029/2020GC008960

Brandt, D., Constable, C., & Ernesto, M. (2020). Giant Gaussian process models of geomagnetic palaeosecular variation: a directional outlook. *Geophysical Journal International*, *222*(3), 1526-1541. doi: 10.1093/gji/ggaa258

Brown, M., Korte, M., Holme, R., Wardinski, I., & Gunnarson, S. (2018). Earth's magnetic field is probably not reversing. *Proceedings of the National Academy of Sciences*, *115*(20), 5111–5116. doi: 10.1073/pnas.1722110115

Christensen, U., & Wicht, J. (2015). 8.10 - numerical dynamo simulations. In G. Schubert (Ed.), *Treatise on geophysics (second edition)* (Second Edition ed., p. 245 - 277). Oxford: Elsevier. doi: https://doi.org/10.1016/B978-0-444-53802-4.00145-7

Christensen, U. R. (2010). Dynamo Scaling Laws and Applications to the Planets. *Space Science Review*, *152*(1-4), 565-590. doi: 10.1007/s11214-009-9553-2

Christensen, U. R., & Aubert, J. (2006). Scaling properties of convection-driven dynamos in rotating spherical shells and application to planetary magnetic fields. *Geophysical Journal International*, *166*(1), 97-114. doi: 10.1111/j.1365-246X.2006.03009.x

Coe, R. S., & Glatzmaier, G. A. (2006). Symmetry and stability of the geomagnetic field. *Geophysical Research Letters*, *33*(21). doi: 10.1029/2006GL027903

Cromwell, G., Johnson, C. L., Tauxe, L., Constable, C. G., & Jarboe, N. A. (2018). Psv10: A global data set for 0–10 ma time-averaged field and paleosecular variation studies. *Geochemistry, Geophysics, Geosystems*, *19*(5), 1533-1558. doi: 10.1002/2017GC007318

Davies, C. J., & Constable, C. G. (2014). Insights from geodynamo simulations into long-term geomagnetic field behaviour. *Earth and Planetary Science Letters*, *404*, 238-249. doi: https://doi.org/10.1016/j.epsl.2014.07.042

Davies, C. J., & Gubbins, D. (2011). A buoyancy profile for the Earth's core. *Geophysical Journal International*, *187*(2), 549-563. doi: 10.1111/j.1365-246X.2011.05144.x

Davies, C. J., Gubbins, D., & Jimack, P. K. (2011). Scalability of pseudospectral methods for geodynamo simulations. *Concurrency and Computation: Practice and Experience*, *23*(1), 38-56. doi: 10.1002/cpe.1593

Driscoll, P., & Olson, P. (2009). Effects of buoyancy and rotation on the polarity reversal frequency of gravitationally driven numerical dynamos. *Geophysical Journal International*, *178*(3), 1337-1350. doi: 10.1111/j.1365-246X.2009.04234.x

Dziewonski, A. M., Lekic, V., & Romanowicz, B. A. (2010). Mantle anchor structure: An argument for bottom up tectonics. *Earth and Planetary Science Letters*, *299*(1), 69 - 79. doi: https://doi.org/10.1016/j.epsl.2010.08.013

Fisher, R. A. (1953). Dispersion on a sphere. *Proceedings of the Royal Society of London. Series A. Mathematical and Physical Sciences*, *217*(1130), 295-305. doi: 10.1098/rspa.1953.0064

Jackson, A., Jonkers, A. R. T., & Walker, M. R. (2000). Four centuries of geomagnetic secular variation from historical records. *Philosophical Transactions of the Royal Society of London. Series A: Mathematical, Physical and Engineering Sciences*, *358*(1768), 957-990. doi: 10.1098/rsta.2000.0569

Korte, M., & Constable, C. (2008). Spatial and temporal resolution of millennial scale geomagnetic field models. *Advances in Space Research*, *41*(1), 57 - 69. doi: https://doi.org/10.1016/j.asr.2007.03.094

Korte, M., Constable, C., Donadini, F., & Holme, R. (2011). Reconstructing the holocene geomagnetic field. *Earth and Planetary Science Letters*, *312*(3), 497 - 505. doi: https://doi.org/10.1016/j.epsl.2011.10.031

Kutzner, C., & Christensen, U. (2000). Effects of driving mechanisms in geodynamo models. *Geophysical Research Letters*, *27*(1), 29-32. doi: 10.1029/1999GL010937

Lhuillier, F., Hulot, G., & Gallet, Y. (2013). Statistical properties of reversals and chrons in numerical dynamos and implications for the geodynamo. *Physics of* *the Earth and Planetary Interiors*, *220*, 19 - 36. doi: https://doi.org/10.1016/j.pepi.2013.04.005

McFadden, P. L., Merrill, R. T., & McElhinny, M. W. (1988). Dipole/quadrupole family modeling of paleosecular variation. *Journal of Geophysical Research: Solid Earth*, *93*(B10), 11583-11588. doi: 10.1029/JB093iB10p11583

Nilsson, A., Holme, R., Korte, M., Suttie, N., & Hill, M. (2014). Reconstructing Holocene geomagnetic field variation: new methods, models and implications. *Geophysical Journal International*, *198*(1), 229-248. doi: 10.1093/gji/ggu120

Nimmo, F. (2015). 8.02 - energetics of the core. In G. Schubert (Ed.), *Treatise on geophysics (second edition)* (Second Edition ed., p. 27 - 55). Oxford: Elsevier. doi: https://doi.org/10.1016/B978-0-444-53802-4.00139-1

Oruba, L., & Dormy, E. (2014). Transition between viscous dipolar and inertial multipolar dynamos. *Geophysical Research Letters*, *41*(20), 7115-7120. doi: 10.1002/2014GL062069

Panovska, S., Constable, C. G., & Korte, M. (2018). Extending global continuous geomagnetic field reconstructions on timescales beyond human civilization. *Geochemistry, Geophysics, Geosystems*, *19*(12), 4757-4772. doi: 10.1029/2018GC007966

Schaeffer, N. (2013). Efficient spherical harmonic transforms aimed at pseudospectral numerical simulations. *Geochemistry, Geophysics, Geosystems*, *14*(3), 751-758. doi: 10.1002/ggge.20071

Schaeffer, N., Jault, D., Nataf, H.-C., & Fournier, A. (2017). Turbulent geodynamo simulations: a leap towards Earth's core. *Geophysical Journal International*, *211*(1), 1-29. doi: 10.1093/gji/ggx265

Sprain, C. J., Biggin, A. J., Davies, C. J., Bono, R. K., & Meduri, D. G. (2019). An assessment of long duration geodynamo simulations using new paleomagnetic modeling criteria (qpm). *Earth and Planetary Science Letters*, *526*, 115758. doi: 10.1016/j.epsl.2019.115758

Tauxe, L., & Kent, D. V. (2004). A simplified statistical model for the geomagnetic field and the detection of shallow bias in paleomagnetic inclinations: was the ancient magnetic field dipolar? In *Timescales of the paleomagnetic field* (p. 101-115). American Geophysical Union (AGU). doi: 10.1029/145GM08

Wardinski, I., & Korte, M. (2008). The evolution of the core-surface flow over the last seven thousands years. *Journal of Geophysical Research: Solid Earth*, *113*(B5). doi: 10.1029/2007JB005024

Wicht, J. (2002). Inner-core conductivity in numerical dynamo simulations. *Physics of the Earth and Planetary Interiors*, *132*(4), 281 - 302. doi: https://doi.org/10.1016/S0031-9201(02)00078-X

Wicht, J., & Meduri, D. G. (2016). A gaussian model for simulated geomagnetic field reversals. *Physics of the Earth and Planetary Interiors*, *259*, 45 - 60. doi: https://doi.org/10.1016/j.pepi.2016.07.007

Wicht, J., Stellmach, S., & Harder, H. (2015). Numerical dynamo simulations: From basic concepts to realistic models. In W. Freeden, M. Z. Nashed, & T. Sonar (Eds.), *Handbook of geomathematics* (pp. 779–834). Berlin, Heidelberg: Springer Berlin Heidelberg. doi: 10.1007/978-3-642-54551-1_16

Wicht, J., & Tilgner, A. (2010). Theory and modeling of planetary dynamos. *Space Science Reviews*, *152*(1), 501 - 542. doi: https://doi.org/10.1007/s11214-010-9638-y

Willis, A. P., Sreenivasan, B., & Gubbins, D. (2007). Thermal core-mantle interaction: Exploring regimes for "locked" dynamo action. *Physics of the Earth and Planetary Interiors*, *165*(1), 83 - 92. doi: https://doi.org/10.1016/j.pepi.2007.08.002

Yadav, R. K., Gastine, T., Christensen, U. R., Wolk, S. J., & Poppenhaeger, K. (2016). Approaching a realistic force balance in geodynamo simulations. *Proceedings of the National Academy of Sciences*, *113*(43), 12065–12070. doi:

10.1073/pnas.1608998113